

SOLAR CELLS

A piperidinium salt stabilizes efficient metal-halide perovskite solar cells

Yen-Hung Lin^{1*}, Nobuya Sakai¹, Peimei Da¹, Jiaying Wu², Harry C. Sansom¹, Alexandra J. Ramadan¹, Suhas Mahesh¹, Junliang Liu³, Robert D. J. Oliver¹, Jongchul Lim[†], Lee Aspitarte⁴, Kshama Sharma⁵, P. K. Madhu⁵, Anna B. Morales-Vilches⁶, Pabitra K. Nayak^{1,5}, Sai Bai⁷, Feng Gao⁷, Chris R. M. Grover³, Michael B. Johnston¹, John G. Labram⁴, James R. Durrant^{2,8}, James M. Ball¹, Bernard Wenger¹, Bernd Stannowski⁶, Henry J. Snaith^{1*}

Longevity has been a long-standing concern for hybrid perovskite photovoltaics. We demonstrate high-resilience positive-intrinsic-negative perovskite solar cells by incorporating a piperidinium-based ionic compound into the formamidinium-cesium lead-trihalide perovskite absorber. With the bandgap tuned to be well suited for perovskite-on-silicon tandem cells, this piperidinium additive enhances the open-circuit voltage and cell efficiency. This additive also retards compositional segregation into impurity phases and pinhole formation in the perovskite absorber layer during aggressive aging. Under full-spectrum simulated sunlight in ambient atmosphere, our unencapsulated and encapsulated cells retain 80 and 95% of their peak and post-burn-in efficiencies for 1010 and 1200 hours at 60° and 85°C, respectively. Our analysis reveals detailed degradation routes that contribute to the failure of aged cells.

Two-terminal monolithic perovskite-on-silicon tandem cells appear to be one of the most promising photovoltaic technologies for near-term commercial-scale deployment (1, 2). These cells feature a wide bandgap perovskite “top cell” that absorbs in a region of the solar spectrum complementary to that of the silicon “bottom cell,” and such solar cells have been demonstrated with a certified power conversion efficiency (PCE) reaching 29.1% (3).

There is often a compromise between achieving high efficiency and long-term stability. The presence of methylammonium (MA) as the A-site cation in the perovskite absorber, which leads to more rapid decomposition under elevated temperature, light exposure, and atmosphere (4), can be alleviated by substitution with formamidinium (FA) or compositions of FA and cesium (Cs) (5–7). However, the use of MA persists in many recent reports on the highest-

efficiency perovskite cells in the form of the mixed-cation CsFAMA or FAMA perovskites (8, 9). Also, the organic hole conductor 2,2',7,7'-tetrakis[*N,N*-di(4-methoxyphenyl)amino]-9,9'-spirobifluorene (Spiro-OMeTAD) and the additives required to deliver high efficiency are detrimental to the stability of perovskite cells (10–12) but are often used in the highest PCE single-junction perovskite cells (9, 12). Finally, molecular passivation of defects in the perovskite absorber is a common route to increase the solar cell efficiency (13) but often introduces additional thermal instabilities. The absorber layers and cells can revert to their unpassivated state after thermal treatment at temperatures as low as 60° to 85°C (9).

Thus, efforts are required to simultaneously deliver efficiency enhancements and improve long-term stability. We recently reported that incorporation of an imidazolium-based ionic liquid into positive-intrinsic-negative (p-i-n) perovskite solar cells, which use the triple cation perovskite as the absorber layer and nickel oxide (NiO) as the p-type layer, can improve both efficiency and long-term stability (14). However, the best-quality NiO p-type layers require annealing at ~400°C, which makes their integration with Si heterojunction bottom cells challenging, because these bottom cells cannot be processed above 200°C owing to the sensitivity of the amorphous silicon passivation and charge extraction layers. We also found that this imidazolium-based ionic liquid is incompatible with the use of low-temperature processible organic p-type layers. Moreover, we carried out thermal stability tests in nitrogen at 85°C and found that, when using NiO p-type layers, the cells were considerably less stable than cells that use poly(4-butylphenyl-diphenylamine)

(polyTPD) as the hole-transport material, which we show in fig. S1.

In this study, we demonstrate high-performance p-i-n perovskite solar cells using thermally stable CsFA-based lead-halide perovskite absorber layers, low-temperature processed organic charge extraction layers, and the organic ionic solid additive 1-butyl-1-methylpiperidinium tetrafluoroborate ([BMP]⁺[BF₄][−]). The incorporation of [BMP]⁺[BF₄][−] into the perovskite absorber suppressed deep trap states, improved performance, and enhanced the operational stability of cells stressed under full-spectrum sunlight at elevated temperatures up to 85°C.

We screened a number of ionic salts as additives for improving the efficiency of perovskite solar cells, with the commonality of having a large chemically stable organic cation and a [BF₄][−] anion. At low concentrations, [BMP]⁺[BF₄][−] (see Fig. 1A for the chemical structure) resulted in a particularly positive influence in photovoltaic performance. We depict the device architecture in Fig. 1A, where polyTPD and [6,6]-phenyl-C₆₁-butyric acid methyl ester (PCBM) were used as the hole-transporting and electron-transporting layers, respectively. The scanning electron microscopy (SEM) image for a representative p-i-n cell based on a perovskite composition of Cs_{0.17}FA_{0.83}Pb(I_{0.77}Br_{0.23})₃ and 0.25 mol % [BMP]⁺[BF₄][−] (with respect to the Pb content) is shown in Fig. 1B.

To demonstrate the performance enhancement potential of [BMP]⁺[BF₄][−], we fabricated mixed halide perovskites with a low Br content Cs_{0.17}FA_{0.83}Pb(I_{0.90}Br_{0.10})₃, which we have found to be the best composition for maximum efficiency of single-junction cells. In Fig. 1C and fig. S2, we show typical current density–voltage (*J*-*V*) characteristics for the 0.25 mol % [BMP]⁺[BF₄][−] modified and control devices, and the statistical results of the device performance parameters are shown in Fig. 1D. A champion [BMP]⁺[BF₄][−] device (Fig. 1E) exhibited an open-circuit voltage (*V*_{OC}) of 1.12 V, a short-circuit current density (*J*_{SC}) of 22.8 mA·cm^{−2}, and a fill factor (FF) of 0.79, resulting in a PCE of 20.1% and a steady-state power output (SPO) of 20.1%. The corresponding external quantum efficiency (EQE) (fig. S3) yielded an integrated *J*_{SC} with a negligible variation (~2.5%) from the measured *J*_{SC}. The addition of [BMP]⁺[BF₄][−] in the perovskite light absorber led to very high performance for MA-free single-junction p-i-n perovskite solar cells compared with reports to date (5, 15).

For a perovskite-on-silicon tandem solar cell, balancing the light absorption between the constituent subcells is key to achieving current matching to maximize PCE (16, 17). Following (17), we simulated the evolution of subcell *J*_{SC} values in perovskite-on-silicon tandem cells as a function of absorber layer thickness for perovskite bandgaps of 1.56, 1.66, and 1.76 eV (Fig. 1F).

¹Clarendon Laboratory, Department of Physics, University of Oxford, Oxford OX1 3PU, UK. ²Department of Chemistry and Centre for Plastic Electronics, Imperial College London, London W12 0BZ, UK. ³Department of Materials, University of Oxford, Oxford OX1 3PH, UK. ⁴School of Electrical Engineering and Computer Science, Oregon State University, Corvallis, OR 97331, USA. ⁵TIFR Centre for Interdisciplinary Sciences, Tata Institute of Fundamental Research, Hyderabad 500107, India. ⁶PVcomB, Helmholtz-Zentrum Berlin für Materialien und Energie GmbH, 12489 Berlin, Germany. ⁷Department of Physics, Chemistry and Biology (IFM), Linköping University, 581 83 Linköping, Sweden. ⁸Sustainable Product Engineering Centre for Innovative Functional Industrial Coatings (SPECIFIC), College of Engineering, Swansea University, Bay Campus, Swansea SA1 8EN, UK.

*Corresponding author. Email: yen-hung.lin@physics.ox.ac.uk (Y.-H.L.); henry.snaith@physics.ox.ac.uk (H.J.S.)

†Present address: Graduate School of Energy Science and Technology, Chungnam National University, Yuseong-gu, Daejeon 34134, Republic of Korea.

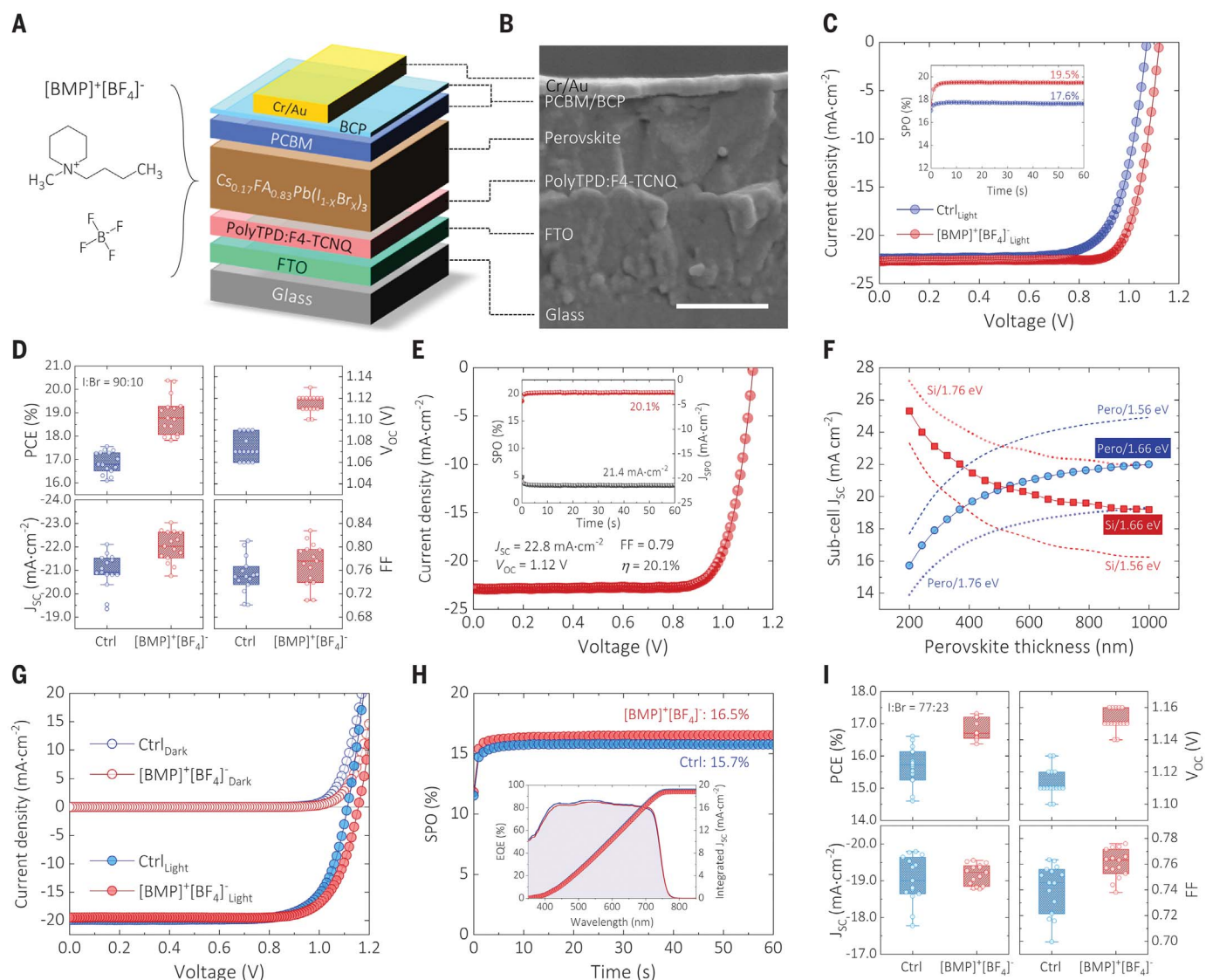


Fig. 1. Perovskite solar cell characterization. (A) Schematic of the p-i-n perovskite solar cell and the chemical structure of [BMP]⁺[BF₄]⁻. BCP, bathocuproine; PCBM, phenyl-C₆₁-butyric acid methyl ester; PolyTPD, poly(4-butylphenyl-diphenylamine); F4-TCNQ, tetrafluoro-7,7,8,8-tetracyanoquinodimethane. (B) SEM image of the full device stack made from Cs_{0.17}FA_{0.83}Pb(I_{0.77}Br_{0.23})₃ with 0.25 mol % [BMP]⁺[BF₄]⁻. Scale bar, 500 nm. (C) J-V characteristics of the representative 0.25 mol % [BMP]⁺[BF₄]⁻ modified Cs_{0.17}FA_{0.83}Pb(I_{0.90}Br_{0.10})₃ and control (Ctrl) devices measured from the forward-bias (FB) to short-circuit (SC) scans under simulated air mass 1.5 sunlight and corresponding SPO. (D) Statistical results of device parameters for Cs_{0.17}FA_{0.83}Pb(I_{0.90}Br_{0.10})₃-based devices. (E) J-V characteristics for the champion

cell with 0.25 mol % [BMP]⁺[BF₄]⁻ modified Cs_{0.17}FA_{0.83}Pb(I_{0.90}Br_{0.10})₃. η , power conversion efficiency. (Inset) corresponding SPO and current density measured under SPO (J_{SPO}). (F) Modeling of the thickness-dependent subcell J_{SC} for perovskite-on-silicon tandem cells with perovskites of different bandgaps. The evolution of perovskite subcell J_{SC} is shown in blue, and the corresponding Si subcell J_{SC} is shown in red. (G) J-V characteristics of the representative 0.25 mol % [BMP]⁺[BF₄]⁻ modified and control devices using Cs_{0.17}FA_{0.83}Pb(I_{0.77}Br_{0.23})₃. (H) Corresponding SPO, EQE, and integrated J_{SC} for the devices shown in (G). The integrated J_{SC} values for the modified and control devices are 18.8 and 19.0 mA·cm⁻², respectively. (I) Statistical results of device parameters for Cs_{0.17}FA_{0.83}Pb(I_{0.77}Br_{0.23})₃-based devices.

The ideal thickness for a 1.66 eV bandgap was ~500 nm, which falls into a common perovskite processing window (15). We also modeled the subcell J_{SC} with various bandgaps for a 500-nm perovskite layer (fig. S4), and a 1.66 eV bandgap was also nearly ideal for maximizing energy yield for monolithic perovskite-on-silicon tandem cells deployed in real-world locations (18).

By tuning the I/Br composition, we found that Cs_{0.17}FA_{0.83}Pb(I_{0.77}Br_{0.23})₃ perovskite delivered the desired 1.66 eV bandgap, as determined from the derivative of the EQE spectrum, (fig. S5). We optimized the single-junction cells using different [BMP]⁺[BF₄]⁻ concentrations ranging from 0.0 (control) to 0.3 mol %; the device performance parameters from a large batch of cells are summarized in fig. S6. With increas-

ing concentrations of [BMP]⁺[BF₄]⁻, we observed that V_{OC} rose from an average of 1.11 V for the control device to >1.16 V for the 0.3 mol % [BMP]⁺[BF₄]⁻ modified device; J_{SC} did not vary appreciably relative to the control. However, on average, the FF increased at low concentrations but tended to decrease at higher concentrations of [BMP]⁺[BF₄]⁻. Thus, devices with 0.25 mol % [BMP]⁺[BF₄]⁻ exhibited the

highest PCEs. Characteristic J - V curves for an optimized 0.25 mol % [BMP]⁺[BF₄]⁻ modified perovskite solar cell and a control device are shown in Fig. 1G, and the corresponding SPOs are shown in Fig. 1H. The corresponding forward and reverse direction J - V scans are shown in Fig. S7. The 0.25 mol % [BMP]⁺[BF₄]⁻ device exhibited a V_{OC} of 1.16 V, a J_{SC} of 19.5 mA·cm⁻², and a FF of 0.77, yielding a PCE of 17.3%. The control device, which exhibited a lower PCE of 16.6%, had a V_{OC} of 1.11 V and a FF of 0.75. The corresponding SPOs were 16.5 and 15.7% for the modified and control devices, respectively. We show a set of statistical results obtained from 15 individual cells of each type in Fig. 1I. The EQE (Fig. 1H, inset) was in good agreement with the J_{SC} measured from the J - V scans (Fig. 1G). With the addition of [BMP]⁺[BF₄]⁻, the cells generally exhibited an increase in V_{OC} , FF, and PCE. The J_{SC} was similar or slightly higher with the optimum piperidinium content for all perovskite compositions.

To understand the impact on the optoelectronic characteristics of the perovskite films with the addition [BMP]⁺[BF₄]⁻, we carried out a series of spectroscopic measurements, including transient photovoltage (TPV) (fig. S8A), charge extraction (fig. S8B), time-resolved photoluminescence (TRPL) (fig. S9A), steady-state photoluminescence (SSPL) (fig. S9B), and transient photoconductivity (TPC) (fig. S10) on half-complete or complete device structures, and time-resolved microwave conductivity (TRMC) (figs. S11 and S12) and in-plane tran-

sient photoconductivity (ip-TPC) (fig. S13) on isolated perovskite films. We found that adding [BMP]⁺[BF₄]⁻ did not compromise charge carrier mobilities (figs. S10B, S12, and S13A). Furthermore, from light intensity-dependent V_{OC} and charge-extraction measurements of complete devices, we observed a reduced ideality factor and capacitance (or reduced total stored charge density) for the [BMP]⁺[BF₄]⁻ modified devices under low light intensity (fig. S8B). We also observed a slower TRPL decay and more than double the SSPL intensity in the [BMP]⁺[BF₄]⁻ film (fig. S9). These results were consistent with a reduced density of deep trap sites in the [BMP]⁺[BF₄]⁻ modified devices. Further analysis of the optoelectronic and spectroscopic characterizations is provided in the supplementary text section of the supplementary materials.

To reveal how [BMP]⁺[BF₄]⁻ was distributed within the perovskite layer, we used high-resolution nanoscale secondary ion mass spectrometry (nanoSIMS). We present the secondary electron and elemental mapping for the ¹⁹F⁻ and ¹¹B¹⁶O₂⁻ distributions in a Cs_{0.17}FA_{0.83}Pb(I_{0.77}Br_{0.23})₃ perovskite film in Fig. 2, A to C. In Fig. 2A, the ¹⁹F⁻ signals show agglomeration and, despite yielding much lower intensities, the ¹¹B¹⁶O₂⁻ intensity map (Fig. 2B) coincided reasonably well with the ¹⁹F⁻ map. We show the three-dimensional (3D) visualization of the entire ¹⁹F⁻ dataset in Fig. 2D, where we observed that the ¹⁹F⁻ signal originated from roughly spherical regions a few hundred nanometers

in diameter that were evenly distributed over the surveyed volume. Both the depth (fig. S14A) and line (fig. S14B) profiles revealed that, in addition to the agglomerates, a small amount of F could be detected throughout the perovskite.

From this nanoSIMS characterization, we deduce that most of the [BMP]⁺[BF₄]⁻ molecules were localized in isolated aggregates that presumably accumulated between the perovskite domains, but small amounts penetrated the entire volume of the film. This distribution differs from that of the imidazolium-based ionic liquid, which we have previously used with NiO p-type layers. For that material, the predominant accumulation of [BF₄]⁻ was at the buried NiO-perovskite interface (14). Presumably, the distribution throughout the entire volume of the perovskite film helped the [BMP]⁺[BF₄]⁻ ionic salt enhance the performance of the cells when we used the poly-TPD organic hole conductor. We attempted to observe interactions between the [BMP]⁺[BF₄]⁻ and the perovskites using solid-state nuclear magnetic resonance (ssNMR) and x-ray photoemission spectroscopy (XPS), which we show in the supplementary text and figs. S15 and S16, respectively. However, we observed no discernible differences between the control and modified samples.

We also carried out characterizations to assess the stability of the CsFA perovskite compounds after the addition of [BMP]⁺[BF₄]⁻. Ultraviolet-visible (UV-vis) absorption spectra (fig. S17) and x-ray diffraction (XRD)

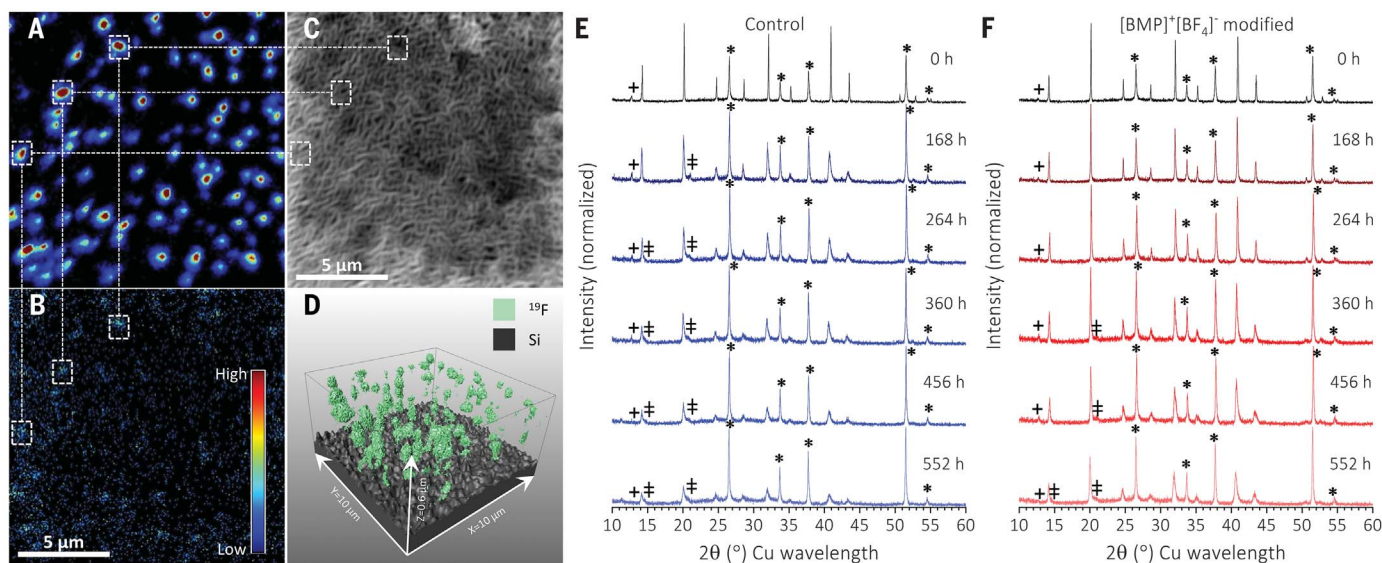


Fig. 2. High-resolution secondary ion mass spectrometry and x-ray diffraction analysis. (A and B) ¹⁹F⁻ and ¹¹B¹⁶O₂⁻ ion maps for the F and B distributions toward the top surface of a ~500-nm Cs_{0.17}FA_{0.83}Pb(I_{0.77}Br_{0.23})₃ with 0.25 mol % [BMP]⁺[BF₄]⁻ perovskite film. (C) Secondary electron map for the sputtered surface morphology ~60 nm below the sample surface. The squares denoted in (A) to (C) are to indicate the corresponding regions of highly localized F and B concentrations. (D) A reconstructed 3D map

(stretched in the z direction for clarity) showing the distribution of the ¹⁹F⁻ signals through the perovskite layer. (E and F) XRD series for the gaining of the unencapsulated control and 0.25 mol % [BMP]⁺[BF₄]⁻ modified Cs_{0.17}FA_{0.83}Pb(I_{0.77}Br_{0.23})₃ perovskite films, respectively, prepared on FTO glass substrates. The XRD peaks corresponding to PbI₂ (+ symbol), FTO (asterisk symbol), and the secondary cubic perovskite phase (‡ symbol) are marked. h, hours.

patterns (Fig. 2, E and F) were obtained for the $[\text{BMP}]^+[\text{BF}_4]^-$ modified and control $\text{Cs}_{0.17}\text{FA}_{0.83}\text{Pb}(\text{I}_{0.77}\text{Br}_{0.23})_3$ perovskite films aged under simulated full-spectrum sunlight at 60°C in ambient air (relative humidity in the laboratory was ~50%). The absorption edge of the $[\text{BMP}]^+[\text{BF}_4]^-$ modified sample exhibited a minor change for the first 264 hours (fig. S17A), whereas the control sample exhibited a clear redshift in the absorption edge, which moved from ~750 nm to >775 nm (fig. S17B). This redshift in absorption also coincides with a redshift in the EQE spectrum of complete solar cells aged in a similar manner (fig. S18), indicating that a similar change is occurring, albeit at a slower rate, in the complete devices. The XRD measurements did not reveal any noticeable formation of lead halide (~12.7°) with aging time for both the control (Fig. 2E) and modified (Fig. 2F) samples, which is usually observed during degradation of MA-containing perovskites because of the loss of methylammonium iodide (4). Conversely, a small PbI_2 peak present at 12.7° in both the control and modified films early on disappeared during aging. During the time series, the main perovskite phase peaks broadened (fig. S19) and decreased in intensity, and additional peaks at 14.6° and 20.7°, as well as a low-angle peak at 11.3°, appeared during long aging in the control film.

The broadening of the main phase can be explained by orthorhombic strain. Before aging, we fit the main perovskite phase to an orthorhombic cell in space group $Pnma$, with lattice parameters of $a = 8.801(1)$ Å, $b = 8.8329(3)$ Å, and $c = 12.4940(5)$ Å and a volume of $971.3(2)$ Å³ for the control film, and $a = 8.8146(3)$ Å, $b = 8.8333(9)$ Å, and $c = 12.4892(9)$ Å for the modified film with a larger volume of $972.4(1)$ Å³. Both are larger than the orthorhombic perovskite $\gamma\text{-CsPbI}_3$ [volume = $947.33(5)$ Å³] (19), indicating the mixed CsFA phase. The lowering of symmetry from cubic to orthorhombic was needed to fit the XRD data well (fig. S20). We refined the orthorhombic unit cell across the aging series and defined the orthorhombic strain as S (%) = $100 \times \sqrt{\left(\frac{\sqrt{2}a}{\sqrt{2}b} - 1\right)^2 + \left(\frac{\sqrt{2}b}{c} - 1\right)^2 + \left(\frac{\sqrt{2}a}{c} - 1\right)^2}$, which we show in fig. S21A. The orthorhombic strain in the control and modified films increased at a similar rate; however, the control sample started with a slightly more orthorhombic phase.

The orthorhombic strain was the only sign of change in the XRD pattern for the $[\text{BMP}]^+[\text{BF}_4]^-$ modified samples at aging times less than 360 hours. Comparison of spectra showed that the orthorhombic strain did not have a large effect on the absorption. The additional peaks at 14.6° and 20.7° appeared for the control sample after the first aging step of 168 hours and for the modified sample between 264 and 360 hours of aging. These peaks were fitted to

a cubic unit cell in the $Pm\bar{3}m$ space group and could not be fitted with the unit cells of any of the relevant binary halide salts. For the modified sample aged at 360 hours, the cubic unit cell has a volume of $217(1)$ Å³, which is within error of the reported volume of FAPbBr_3 [$217.45(2)$ Å³] (20). The XRD peaks associated with this second phase are indicated with the ‡ symbol in Fig. 2, E and F, and fig. S22.

Segregation of FAPbBr_3 would leave the main phase rich in Cs and I. Iodide enrichment was consistent with the redshift seen in absorption spectra (fig. S17), and the time at which these phases emerged in the XRD patterns coincides with the timing for the redshift. The volume of the main orthorhombic perovskite phase and the secondary FAPbBr_3 perovskite phase both initially increased over time but started to decrease for the control after the 264-hour aging (fig. S21, B and C). This decrease suggests that after the initial separation of FAPbBr_3 , other compositional changes continued, either because of mixing of the halides or external factors. At the same time, the intensity of the main phase peaks decreased, and the decrease was faster in the control sample. The peak at 11.3°, which appeared in the control sample after 456 hours (fig. S23) but was suppressed in the modified sample, was previously ascribed to the nonperovskite yellow hexagonal $\delta\text{-FAPbI}_3$ phase (21, 22), which can form in the perovskite film when the Cs or FA content is strongly unbalanced (7, 21, 23).

In an attempt to visualize the impurity phases generated during aging, we performed optical microscopy measurements on the fresh and aged control (fig. S24) and $[\text{BMP}]^+[\text{BF}_4]^-$ modified (fig. S25) $\text{Cs}_{0.17}\text{FA}_{0.83}\text{Pb}(\text{I}_{0.77}\text{Br}_{0.23})_3$ perovskite films grown on fluorine-doped tin oxide (FTO) glass. The aged samples were subjected to 500 hours of the same aging environmental parameters that were applied to the XRD samples. The microscope was backlit with a halogen lamp, with optional additional photoexcitation from the front with a 375-nm UV light-emitting diode (LED) to induce photoluminescence. Both the fresh control and $[\text{BMP}]^+[\text{BF}_4]^-$ modified films appeared orange-red in color and had wrinkled surface characteristic of the anti-solvent quenching spin-coating fabrication method (24) and showed no clear difference with or without UV illumination. After aging, the $[\text{BMP}]^+[\text{BF}_4]^-$ modified films appeared to be predominantly unchanged.

In contrast, for the control films, we observed a strong darkening in color and the appearance of large dark domains. Upon UV illumination, these dark domains emitted blue light. The blue emission was consistent with these regions containing some wider gap impurity phase material, most likely the nonperovskite hexagonal $\delta\text{-FAPbI}_3$ phase (21, 22). In addition to these coarse features, we observed numerous white or yellow bright spots

in images of the aged control samples (fig. S24, C to F). From SEM images of the same samples, which we present in fig. S26, we confirmed that these bright spots were pinholes in the film. The presence of these pinholes in the aged control films, which were absent from the $[\text{BMP}]^+[\text{BF}_4]^-$ modified films, was a key difference. The addition of $[\text{BMP}]^+[\text{BF}_4]^-$ appeared to have prevented the formation of the blue-emitting impurity phase, inhibited FAPbBr_3 impurity phase growth, and strongly suppressed pinhole formation (fig. S26D).

We investigated the operational stability of $\text{Cs}_{0.17}\text{FA}_{0.83}\text{Pb}(\text{I}_{0.77}\text{Br}_{0.23})_3$ -based perovskite solar cells aged at open-circuit condition under full-spectrum sunlight at elevated temperatures in ambient air (relative humidity in the laboratory was ~50%). We first examined the stability of unencapsulated devices aged at 60°C. The average SPOs and PCEs obtained from eight individual devices for each condition are shown in Fig. 3, A and B, respectively, and the evolution of the device parameters is plotted in fig. S27. For both the $[\text{BMP}]^+[\text{BF}_4]^-$ modified and control devices, we observed a positive light-soaking effect that enhanced the SPO and PCE values by ~2% absolute during the first few days of aging, whereas the average SPO and PCE of the control devices dropped below the initial performance after 72 hours and continuously decreased to ~5% absolute efficiency after 216 hours. The efficiency of the $[\text{BMP}]^+[\text{BF}_4]^-$ modified devices improved over the first few hundred hours, likely because of the photo-brightening effect (25) resulting from passivation of defects in the perovskite film via reaction with photogenerated superoxide and peroxide species (26).

Our $[\text{BMP}]^+[\text{BF}_4]^-$ modified devices remained highly operational, decreasing to 80% of the peak SPO and PCE ($T_{80,\text{ave}}$) within an average time of 944 and 975 hours, respectively. We observed that the V_{OC} remained beyond its initial level for >1000 hours at close to 1.2 V (fig. S27A). The unencapsulated devices appear to be much more stable than the isolated perovskite films aged under the same conditions. This is likely because of the PCBM and BCP electron extraction layer and the CrAu electrode partially encapsulating the perovskite film, by inhibiting ingress of atmosphere and loss of degradation products (10, 27–29). Our champion $[\text{BMP}]^+[\text{BF}_4]^-$ device exhibited the measured and estimated lifetimes through a linear extrapolation for 80% of the peak SPO and PCE (i.e., $T_{80,\text{champ}}$) of 1010 and 2630 hours, respectively (30). The difference in $T_{80,\text{champ}}$ between SPO and PCE originates from non-negligible hysteresis in the J - V scans from the aged samples (fig. S28). We benchmark our stability results against the long-term stability data from the literature (table S1). Most stability studies are performed on encapsulated cells or cells in an inert atmosphere. Previous reports

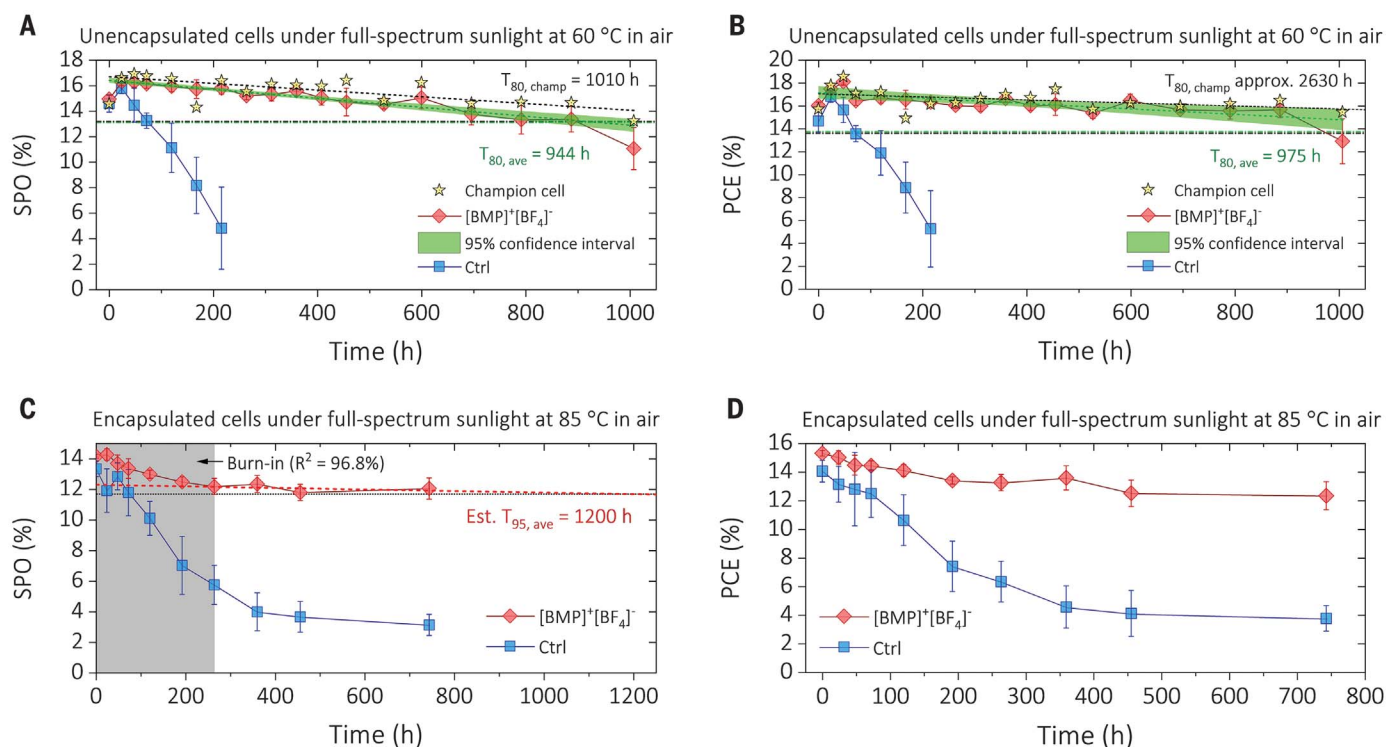


Fig. 3. Long-term operational stability. (A) Evolution of SPOs of unencapsulated 0.25 mol % [BMP]⁺[BF₄]⁻ modified and control (Ctrl) Cs_{0.17}FA_{0.83}Pb(I_{0.77}Br_{0.23})₃ perovskite solar cells (eight cells for each condition), aged under full-spectrum sunlight at 60 °C in ambient air. The 95% confidence interval for the SPOs of the modified devices is shown as a green band. The champion cell with the [BMP]⁺[BF₄]⁻ additive is indicated with yellow stars, and the black dotted line is a guide to the eye. The intersections between the data points and the black and green dashed-dotted lines show $T_{80, \text{champ}}$ for the champion cell and $T_{80, \text{ave}}$ for eight individual

cells, respectively. (B) Corresponding PCEs for (A). (C) Evolution of SPOs of encapsulated 0.25 mol % [BMP]⁺[BF₄]⁻ modified and control Cs_{0.17}FA_{0.83}Pb(I_{0.77}Br_{0.23})₃ cells aged under full-spectrum sunlight at 85 °C in ambient air (six cells for each condition). The early burn-in region (~264 hours) is determined using a linear model (coefficient of determination $R^2 = 96.8\%$). The intersection between the linear extrapolation for the data (red dashed line) and black dotted line estimated the lifetime for 95% of the post-burn-in SPO (Est. $T_{95, \text{ave}}$) from six individual cells. (D) Corresponding PCEs for (C). In all figures, the error bars denote standard deviations.

from unencapsulated cells in ambient atmosphere have delivered T_{80} of ~100 hours under similar aging conditions (14), or similar T_{80} lifetimes, but at 25 °C in Colorado at a relative humidity of 15%, dropping to ~30 hours at 70 °C (12).

To explore the stability of our cells under higher elevated temperatures, we sealed them in a nitrogen atmosphere with glass cover slides and UV-cured epoxy resin and aged the encapsulated devices under full-spectrum sunlight at 85 °C in air. Figure S29 shows the evolution of the device parameters. The J - V scans for the champion [BMP]⁺[BF₄]⁻ device at different aging stages are shown in fig. S30. At this temperature, a clear burn-in effect was observed in the SPOs (Fig. 3C) and PCEs (Fig. 3D) for both the [BMP]⁺[BF₄]⁻ modified and control devices. The SPO of the control devices decreased rapidly to <6% absolute efficiency after 264 hours, whereas the modified devices retained an operational SPO of ~12% absolute over the aging period. We estimated the lifetime of 1200 hours at 95% of the post-burn-in efficiency ($T_{95, \text{ave}}$), using a linear extrapolation of the post-burn-in SPO (Fig. 3C) (14, 30).

Much variation in aging conditions for perovskite solar cells occurs between laboratories, so it is not feasible to compare results directly. With respect to our previous best-in-class, the T_{80} lifetime of our unencapsulated cells at 60 °C in this study is ~7 times longer (14). The post-burn-in $T_{95, \text{ave}}$ SPO lifetime of our encapsulated cells at 85 °C was 1200 hours, three times longer than our previous best-in-class cells, which were stressed at 75 °C and gave a $T_{95, \text{ave}}$ of ~360 hours (14). Considering that we would expect about a twofold increase in the degradation rate with a 10 °C increase in temperature (31), the cells in this study appear to degrade at approximately one sixth the speed.

To elucidate the degradation mechanism in complete cells, we carried out XPS analysis on the unencapsulated device stacks, absent of electrodes, before and after a 300-hour light-soaking aging process at 60 °C. The XPS spectra of the core levels relevant to the perovskite elements were measured, and full peak positions, spectra, and fittings can be found in figs. S31 to S33 and table S2. Subtle differences between the [BMP]⁺[BF₄]⁻ and control devices

were observed in the C 1s, N 1s core levels, but these additional peaks correspond to the presence of [BMP]⁺[BF₄]⁻. The I 3d_{5/2} core levels for both the [BMP]⁺[BF₄]⁻ and control devices show that aging resulted in the emergence of an additional peak at ~620 eV next to the main peak at ~618 eV, which is attributed to I⁻. This peak at the higher binding energy could correspond to either the formation of IO₂⁻, which has been previously observed in methylammonium lead triiodide (32), or to the formation of methyl iodide (33).

The Pb 4f core level spectra demonstrated a clear difference between the aged devices with and without [BMP]⁺[BF₄]⁻. In the aged control devices, we observed two peaks at 138.0 and 139.1 eV (Pb 4f_{7/2}), whereas in the devices with [BMP]⁺[BF₄]⁻ we only observed one peak at 137.8 eV. The peaks at ~138 eV correspond to the presence of Pb²⁺, while the peak at 139.1 eV corresponds to PbO_x. This result suggests that, when aged, the control devices formed lead oxide, which is a product formed from a photooxidative degradation process (34). The addition of [BMP]⁺[BF₄]⁻ inhibited lead oxidation.

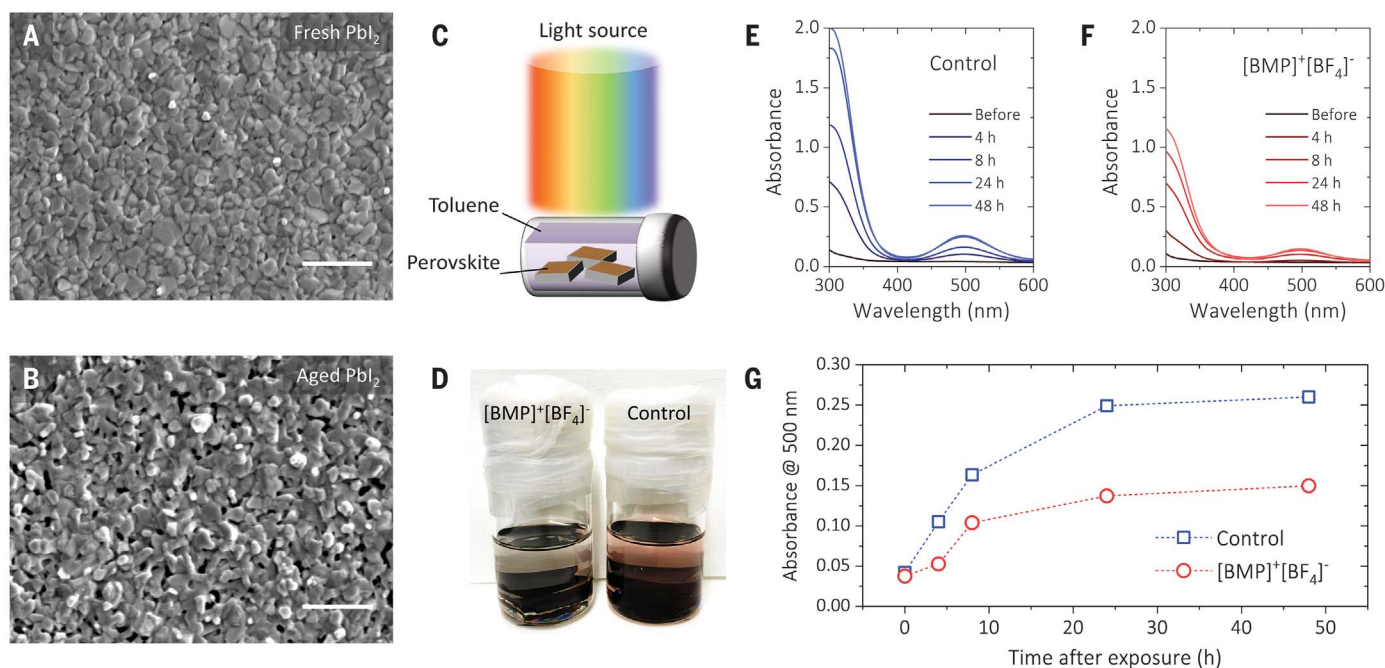


Fig. 4. Iodine-loss analysis of PbI_2 and perovskite films. (A and B) Top-surface SEM images of PbI_2 films: (A) fresh and (B) aged under ~ 0.32 suns white LED illumination at 85°C in a nitrogen-filled glove box for 6 hours. Scale bars, 1 μm . (C) Schematic of the iodine-loss experimental setup: Vials filled and sealed in nitrogen, containing perovskite films fully submerged in toluene, were exposed to full-spectrum sunlight at 60°C in

ambient air. (D) Photo of the sealed vials with the control and 0.25 mol % $[\text{BMP}]^+[\text{BF}_4]^-$ additive modified $\text{Cs}_{0.17}\text{FA}_{0.83}\text{Pb}(\text{I}_{0.77}\text{Br}_{0.23})_3$ perovskite samples, taken after 4 hours of light and heat exposure. (E and F) Ten UV-vis absorbance spectra recorded for the toluene solution taken from the (E) control and (F) $[\text{BMP}]^+[\text{BF}_4]^-$ vials at different aging times. (G) Evolution of absorbance recorded at 500 nm.

To understand how $[\text{BMP}]^+[\text{BF}_4]^-$ can improve the stability of the perovskite film, we first review the mechanisms that have been proposed to explain the photoinduced degradation processes of metal halide perovskites. The role of oxygen and moisture has been extensively discussed, in particular for MA-containing perovskites (35–37). However, for perovskite films prepared in inert atmosphere and encapsulated, photodegradation is still observed. A key factor in the photodegradation is the generation of I_2 under illumination, which has been observed experimentally via a range of analytic methods, including electrochemistry (38), optical absorption (38), and mass spectrometry (39). The detrimental role of I_2 has been established for silver electrodes (40) but also directly upon the perovskite (41).

Several mechanisms have been proposed to explain the generation of I_2 . They have in common the capture of a hole by an iodide ion (I^-), with I^- being either in its lattice site ($\text{I}_\text{l}^- + \text{h}^+ \rightarrow \text{I}_\text{l}^\bullet$ in Kröger-Vink notation) (26, 42), as an interstitial ion from a Frenkel pair ($\text{I}_\text{i}^- + \text{h}^+ \rightarrow \text{I}_\text{i}^\bullet$) (43), or becoming interstitial upon hole capture ($\text{I}_\text{l}^- + \text{h}^+ \rightarrow \text{I}_\text{i}^\bullet + \text{V}_\text{l}^-$) (38). To generate gaseous iodine (I_2), two neutral atoms ($\text{I}_\text{l}^\bullet$ or $\text{I}_\text{i}^\bullet$) need to diffuse and combine. Owing to the ability to release iodine from the surface of the film, and the likelihood of a higher vacancy density at the surface than in the bulk

of the grains, this process is more likely to happen at the surface of the grains, leading to the release of iodine and the generation of a pair of iodide vacancies (2V_l^-).

The exact nature of the detrimental effect of I_2 on the perovskite is still under debate (41). Fu *et al.* investigated these effects in detail and found that PbI_2 was more prone to degradation than the perovskite itself and that voids were left in the films of PbI_2 upon prolonged exposure to light and heat (44). We repeated Fu *et al.*'s experiments for the photodegradation of PbI_2 at elevated temperatures under light in a nitrogen atmosphere (figs. S34 and S35) and confirmed the observed generation of lead (fig. S36) and pinholes in the films (Fig. 4, A and B). Although slower than for MA^+ -containing perovskites, this degradation pathway was also observed in FACs perovskites, indicating that the I_2 generation process is related to the lead-halide framework.

We confirmed a faster release of I_2 from our control perovskite films versus the $[\text{BMP}]^+[\text{BF}_4]^-$ modified films during light soaking, from UV-vis absorption spectrum of toluene, after exposing toluene-submerged films to light and heat (Fig. 4, C to G) (38, 41). The presence of voids (or pinholes, Fig. 4B) in the PbI_2 films (and control perovskite films, fig. S26) after aging can be explained by the loss of volume during I_2 release, upon conversion to metallic

lead. The presence of PbO_x in the degraded unencapsulated devices (fig. S32) is also consistent with the formation of metallic lead, with subsequent oxidation to PbO_x or $\text{Pb}(\text{OH})_2$ in ambient air, which both have a much higher density than the perovskite.

In light of this degradation mechanism, we discuss the stabilization induced by the ionic additive. For degradation to occur, hole-trapping is likely to require interstitial I^- (43), and two neutral interstitial iodine atoms need to diffuse together and combine to form I_2 . Therefore, this reaction could be slowed by either reducing the overall density of Frenkel defects (iodide vacancies and/or interstitial pairs) or by reducing the diffusivity of interstitials. As with most crystalline materials, defect densities are usually highest on the crystal surface (45). Therefore, we would expect the interstitials or Frenkel defects to mostly diffuse around the surfaces of the polycrystalline domains, where the highest density of defects exists.

If crystallization in the presence of $[\text{BMP}]^+[\text{BF}_4]^-$ leads to reduced Frenkel defect densities, then this would have the effect of reducing the number of sites available for iodide oxidation. Furthermore, if $[\text{BMP}]^+[\text{BF}_4]^-$ adsorbs to these surface defects, it is likely to block or inhibit the further migration of such defects, slowing down the diffusivity of interstitial iodide or neutral iodine interstitials, reducing

the rate of I_2 formation. Finally, $[BMP]^+ [BF_4]^-$ does appear to reduce the amount of residual PbI_2 in the films, by improving the crystallization (as indicated in Fig. 2). Because I_2 generation occurs preferentially at PbI_2 sites (44), minimizing the amount of residual PbI_2 may play a crucial role.

REFERENCES AND NOTES

- W. Chen *et al.*, *Adv. Mater.* **30**, e1800515 (2018).
- T. Leijtens, K. A. Bush, R. Prasanna, M. D. McGehee, *Nat. Energy* **3**, 828–838 (2018).
- The National Renewable Energy Laboratory, Best Research-Cell Efficiency Chart; www.nrel.gov/pv/cell-efficiency.html.
- S. N. Habisreutinger, D. P. McMeekin, H. J. Snaith, R. J. Nicholas, *APL Mater.* **4**, 091503 (2016).
- D. P. McMeekin *et al.*, *Science* **351**, 151–155 (2016).
- G. E. Eperon *et al.*, *Energy Environ. Sci.* **7**, 982–988 (2014).
- J.-W. Lee *et al.*, *Adv. Energy Mater.* **5**, 1501310 (2015).
- M. Saliba *et al.*, *Energy Environ. Sci.* **9**, 1989–1997 (2016).
- Q. Jiang *et al.*, *Nat. Photonics* **13**, 460–466 (2019).
- S. N. Habisreutinger *et al.*, *Nano Lett.* **14**, 5561–5568 (2014).
- Y. Hou *et al.*, *Science* **358**, 1192–1197 (2017).
- J. A. Christians *et al.*, *Nat. Energy* **3**, 68–74 (2018).
- S. N. Habisreutinger, N. K. Noel, H. J. Snaith, R. J. Nicholas, *Adv. Energy Mater.* **7**, 1601079 (2017).
- S. Bai *et al.*, *Nature* **571**, 245–250 (2019).
- S. H. Turren-Cruz, A. Hagfeldt, M. Saliba, *Science* **362**, 449–453 (2018).
- E. Köhnen *et al.*, *Sustain. Energy Fuels* **3**, 1995–2005 (2019).
- L. Mazzarella *et al.*, *Adv. Energy Mater.* **9**, 1803241 (2019).
- M. T. Hörantner, H. J. Snaith, *Energy Environ. Sci.* **10**, 1983–1993 (2017).
- R. J. Sutton *et al.*, *ACS Energy Lett.* **3**, 1787–1794 (2018).
- S. Govinda *et al.*, *J. Phys. Chem. C* **122**, 13758–13766 (2018).
- W. Rehman *et al.*, *Energy Environ. Sci.* **10**, 361–369 (2017).
- Z. Li *et al.*, *Chem. Mater.* **28**, 284–292 (2016).
- C. Yi *et al.*, *Energy Environ. Sci.* **9**, 656–662 (2016).
- K. A. Bush *et al.*, *ACS Energy Lett.* **3**, 1225–1232 (2018).
- D. W. deQuilettes *et al.*, *Nat. Commun.* **7**, 11683 (2016).
- J. S. W. Godding *et al.*, *Joule* **3**, 2716–2731 (2019).
- K. A. Bush *et al.*, *Nat. Energy* **2**, 17009 (2017).
- M. Kaltenbrunner *et al.*, *Nat. Mater.* **14**, 1032–1039 (2015).
- R. Prasanna *et al.*, *Nat. Energy* **4**, 939–947 (2019).
- M. V. Khenkin *et al.*, *Nat. Energy* **5**, 35–49 (2020).
- H. J. Snaith, P. Hacke, *Nat. Energy* **3**, 459–465 (2018).
- G. Rajendra Kumar *et al.*, *Phys. Chem. Chem. Phys.* **18**, 7284–7292 (2016).
- X. L. Zhou, F. Solymosi, P. M. Blass, K. C. Cannon, J. M. White, *Surf. Sci.* **219**, 294–316 (1989).
- Y. X. Ouyang *et al.*, *J. Mater. Chem. A* **7**, 2275–2282 (2019).
- R. Brenes, C. Eames, V. Bulović, M. S. Islam, S. D. Stranks, *Adv. Mater.* **30**, e1706208 (2018).
- Z. Andaji-Garmaroudi, M. Anaya, A. J. Pearson, S. D. Stranks, *Adv. Energy Mater.* **10**, 1903109 (2020).
- N. Aristidou *et al.*, *Nat. Commun.* **8**, 15218 (2017).
- G. Y. Kim *et al.*, *Nat. Mater.* **17**, 445–449 (2018).
- Z. N. Song *et al.*, *Sustain. Energy Fuels* **2**, 2460–2467 (2018).
- Y. Kato *et al.*, *Adv. Mater. Interfaces* **2**, 1500195 (2015).
- S. Wang, Y. Jiang, E. J. Juarez-Perez, L. K. Ono, Y. Qi, *Nat. Energy* **2**, 16195 (2016).
- J. Verwey, J. Schoonman, *Physica* **35**, 386–394 (1967).
- S. G. Motti *et al.*, *Nat. Photonics* **13**, 532–539 (2019).
- F. Fu *et al.*, *Energy Environ. Sci.* **12**, 3074–3088 (2019).
- A. Pimpinelli, J. Villain, *Physics of Crystal Growth* (Cambridge Univ. Press, 2010).

ACKNOWLEDGMENTS

Y.-H.L. thanks N. Noel and W. Li from the University of Oxford (UK) for the discussion on the effect of ionic molecules on perovskites and for assisting with ssNMR sample preparation and optical microscopic imaging, respectively. J. Liu acknowledges the assistance of J. Marrow from the University of Oxford (UK), who provided access to the Avizo software packages to perform 3D virtualization of the nanoSIMS data. **Funding:** This work was supported by the U.K. Engineering and Physical Sciences Research Council (EPSRC) grants EP/S004947/1 and EP/P006329/1. J. Liu and C.R.M.G. are grateful for support for the nanoSIMS facility from EPSRC under grant EP/M018237/1. S.M. is grateful for the support of the

Rhodes Scholarship (India and Worcester). R.D.J.O. gratefully acknowledges the Penrose Scholarship for funding his studentship. **Author contributions:** Y.-H.L. and H.J.S. conceived of the concept, designed the experiments, analyzed the data, and wrote the manuscript. H.J.S. supervised and guided the project. Y.-H.L. performed the fabrication, optimization, and characterization of the perovskite films and solar cells. Y.-H.L. conducted optical microscopy measurements. Y.-H.L. and N.S. conducted UV-vis, XRD, and FTIR characterization and analysis. N.S. performed SEM characterization and material analysis. P.D. and S.B. screened ionic additives and conducted early assessments for single-junction cells. Y.-H.L. and P.D. performed cell thermal-stability measurement on p-type layers. J.W. conducted CE, TPV, and TPC and analyzed the data with J.R.D. H.C.S. conducted analysis on XRD results to deduce degradation mechanism with Y.-H.L. and N.S. A.J.R. performed XPS characterization and analyzed the data with Y.-H.L. and N.S. S.M. performed numerical modeling. J. Liu conducted nanoSIMS characterization and analyzed the results with Y.-H.L., P.K.N., and C.R.M.G. R.D.J.O. conducted EQE measurements and analyzed the data with M.B.J. J. Lim conducted ip-TPC characterization. L.A. and J.G.L. performed TRMC characterization. K.S. and P.K.M. performed ssNMR and analyzed the data with P.K.N. A.B.M.-V. and B.S. contributed to the planning of the experiments to tune the bandgap of the perovskite solar cells and optical modeling. B.W. contributed to degradation mechanism analysis. J.M.B. set up N_2 aging system, characterized the EQE spectrum of aged devices, and evaluated spectrum mismatch factors. Y.-H.L. analyzed the data with H.J.S. F.G. provided suggestions for ionic additives. All authors discussed the results and contributed to the writing of the paper.

Competing interests: H.J.S. is a cofounder, chief scientific officer, and a director of Oxford PV Ltd. Oxford University has filed a patent related to the subject matter of this manuscript. **Data and materials availability:** All data needed to evaluate the conclusions of the paper are present in the paper or the supplementary materials.

SUPPLEMENTARY MATERIALS

science.sciencemag.org/content/369/6499/96/suppl/DC1
Materials and Methods
Supplementary Text
Figs. S1 to S36
Tables S1 to S2
References (46–80)

10 November 2019; accepted 5 May 2020
10.1126/science.aba1628

A piperidinium salt stabilizes efficient metal-halide perovskite solar cells

Yen-Hung Lin Nobuya Sakai Peimei Da Jiaying Wu Harry C. Sansom Alexandra J. Ramadan Suhas Mahesh Junliang Liu Robert D. J. Oliver Jongchul Lim Lee Aspitarte Kshama Sharma P. K. Madhu Anna B. Morales Vilches Pabitra K. Nayak Sai Bai Feng Gao Chris R. M. Grovenor Michael B. Johnston John G. Labram James R. Durrant James M. Ball Bernard Wenger Bernd Stannowski Henry J. Snaith

Science, 369 (6499), • DOI: 10.1126/science.aba1628

Stable perovskites with ionic salts

Ionic liquids have been shown to stabilize organic-inorganic perovskite solar cells with metal oxide carrier-transport layers, but they are incompatible with more readily processible organic analogs. Lin *et al.* found that an ionic solid, a piperidinium salt, enhanced the efficiency of positive-intrinsic-negative layered perovskite solar cells with organic electron and hole extraction layers. Aggressive aging testing showed that this additive retarded segregation into impurity phases and pinhole formation in the perovskite layer.

Science, this issue p. 96

View the article online

<https://www.science.org/doi/10.1126/science.aba1628>

Permissions

<https://www.science.org/help/reprints-and-permissions>

Use of this article is subject to the [Terms of service](#)